Optics Letters

Tailoring diffraction of light carrying orbital angular momenta

Denis A. Ikonnikov[1] and Andrey M. Vyunishev[1,2,*]

[1]Kirensky Institute of Physics, Federal Research Center KSC SB RAS, Krasnoyarsk, 660036, Russia
[2]Institute of Engineering Physics and Radio Electronics, Siberian Federal University, Krasnoyarsk, 660041, Russia
*Corresponding author: vyunishev@iph.krasn.ru

Received 24 January 2020; revised 30 May 2020; accepted 15 June 2020; posted 15 June 2020 (Doc. ID 389019); published 9 July 2020

A unified approach to controlling the diffraction of light carrying orbital angular momenta (OAM) is developed and experimentally verified in this Letter. This approach allows one to specify not only the number of diffraction maxima, their spatial frequencies, and the intensity distribution between them, but also the OAM in each maximum. It is verified that the approach can be used for structuring both single and multiple beams carrying OAMs. Simulations reveal phase singularities in structured beams. In addition, the approach makes it possible to shape the light in regular and irregular two-dimensional arrays with addressing the OAMs at each site. This approach offers new opportunities for singular optics.

https://doi.org/10.1364/OL.389019

The light beams carrying the orbital angular momentum (OAM) $l\hbar$ per photon are the beams with an azimuthal phase dependence of $\exp(il\phi)$ [1–3], where $\hbar$ is the Planck's constant divided by 2π. They are also known as optical vertices, which appear as isolated zero-intensity spots possessing the topological charges l of a helical phase. They can be simply formed by imposing an $\exp(il\phi)$ phase mask onto a Gaussian laser beam by using spatial light modulators [4,5], spiral phase plates [6], q-plates [7], etc. The OAM carrying light beams are promising for optical manipulations (optical tweezers) [8–11], in which the angular momentum of light is converted to the particle momentum, high-resolution imaging [12,13], high-dimensional quantum cryptography [14], and optical communications [15–20]. Depending on the topological charge l of the helical phase, the OAM beams can be quantified as different orthogonal states. Since the OAM states depend on neither the wavelength nor the polarization, OAM carrying beams can be used to enhance the information capacity of optical channels by OAM multiplexing [17,19]. More recently, it was reported on generation of single beams with a superposition of the orbital angular momenta [21,22]. In recent work [23], a simple analytical method of diffraction pattern formation was elaborated and experimentally proved. This approach makes it possible to form a discrete diffraction pattern consisting of a set of fixed-order diffraction maxima using a quasiperiodic diffraction grating. This method can be extended to the case of diffraction of the light beams carrying the OAM. In [24], a quasi-periodic structure with the one-dimensional (1D) long-range translational symmetry characterized by a pair of fixed spatial constants and topological charges was investigated. As shown in [25], four sets of spatial periods and OAMs are promising for free-space multicasting, in which digital signals are encoded to a time-varying series of different OAM states in each diffraction order and transmitted from a transmitter to multiple receivers. A special interest in the field represents creation of two-dimensional (2D) arrays of OAM beams [26,27]. Although the creation of 2D arrays of OAM beams is in progress, the ongoing method of their construction is quite complicated and adopted for creation of regular arrays only. Therefore, it is important to develop a simple and straightforward method to tailor a desired diffraction pattern of light beams carrying a single OAM or superposition of the OAMs with or without 1D or 2D translation symmetry.

In this Letter, a unified approach to tailor diffraction of the light beams carrying the OAMs is developed and experimentally verified. This approach allows one to create 1D and 2D spatial arrays of light beams by addressing the OAM states. A limit case of the high-dimensional multiplication of a light beam with a specific OAM state is considered. This approach may provide new opportunities for structuring light with optical singularities.

To design a light beam with desired spatial characteristics, a phase mask was imposed onto a Gaussian laser beam. The complex modulation function of an arbitrary phase mask (hologram) is

$$t(\mathbf{r}, \phi) = e^{-i\Phi(\mathbf{r},\phi)}, \tag{1}$$

where $\Phi(\mathbf{r}, \phi)$ is the phase modulation function, $\mathbf{r} \in (x, y)$ is the radius vector, and ϕ is the azimuth angle.

The phase modulation function of the binary hologram can be described as

$$\Phi(\mathbf{r}, \phi) = \Phi_0 + \Delta\Phi \cdot \mathrm{sgn}\left(\sum a_n \cos\left[\mathbf{G}_n\mathbf{r} + l_n\phi\right]\right). \tag{2}$$

Here, Φ_0 is the average phase, $\Delta\Phi$ is the maximum deviation of the phase from its average value Φ_0, a_n is the amplitude of the n^{th} spatial harmonic, $\mathbf{G}_n$ is the reciprocal lattice vector (RLV), l_n is the topological charge, and $\mathrm{sgn}(\psi) = |\psi|/\psi$ is the signum function of the argument ψ. The terms $\cos(\mathbf{G}_n)$ provide a

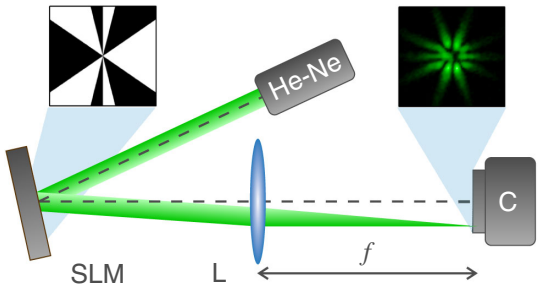

Fig. 1. Schematic of the experimental setup: helium–neon laser, He–Ne; spatial light modulator, SLM; lens, L; and CCD camera C.

long-range translational symmetry, while l_n can be considered as topological defects.

In the proof-of-concept experiments, we used the experimental setup shown in Fig. 1. The binary phase modulation (BPM) pattern was calculated using Eq. (2) and loaded into a 2D phase-only spatial light modulator (SLM, PLUTO-NIR-011, Holoeye, the spatial resolution is 1920 × 1080 pixels, and the pixel pitch is 8 μm). The SLM active area was illuminated by the He–Ne laser radiation ($\lambda = 543$ nm and a full width at half maximum of 544 μm). The diffraction pattern was projected by a lens with $f = 10$ cm onto a CCD matrix of a laser beam profiler (LBP-1, Newport, the pixel sizes are 9.05×8.3 μm^2).

In the degenerate case [$\mathbf{G}_n = 0$ in Eq. (2) for all n], only zero order will appear, and the intensity distribution will depend on the topological charges l_n. Figures 2 and 3 present the numerically calculated and experimental intensity profiles for the beam corresponding to two terms under the sum in Eq. (2). The intensity distribution in the far-field was calculated using the Fresnel–Kirchhoff diffraction equation [28]. It can be seen that the calculated intensity distributions are in good agreement with the experimental results. All the phase masks in Figs. 2 and 3 have the horizontal symmetry (due to the parity of the cosine function) and, therefore, all the corresponding intensity distributions obey such a symmetry. In addition, some of phase masks have a vertical inversion axis [see, e.g., Figs. 2(c) and 2(d)], which determines the symmetry axis of the corresponding intensity distribution. In addition, for the low

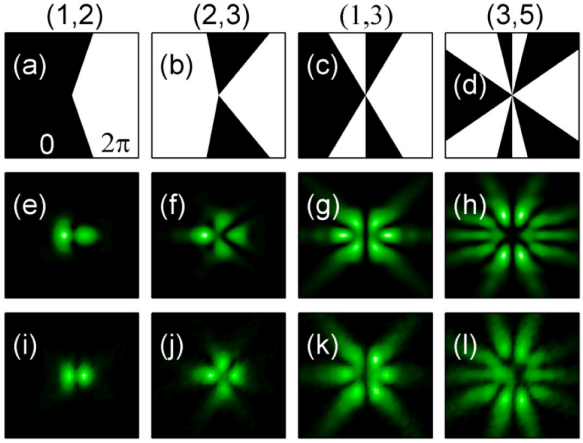

Fig. 2. Binary phase modulation patterns (a)–(d), calculated (e)–(h), and experimental (i)–(l) diffraction patterns for $G_1 = G_2 = 0$ rad · μm^{-1} and (l_1, l_2): (e, i) (1, 2); (f, j) (2, 3); (g, k) (1, 3); and (h, l) (3, 5).

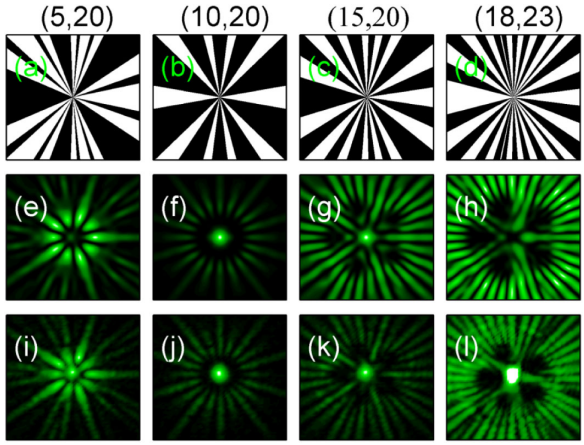

Fig. 3. Binary phase modulation patterns (a)–(d), calculated (e)–(h), and experimental (i)–(l) diffraction patterns for $G_1 = G_2 = 0$ rad · μm^{-1} and (l_1, l_2): (e, i) (5, 20); (f, j) (10, 20); (g, k) (15, 20); and (h, l) (18, 23).

orbital momenta (Fig. 2), the number of azimuthal intensity minima and maxima exactly corresponds to the number of 2π increments on the phase mask. For the higher orbital angular momenta (Fig. 3), the intensity distributions resemble the diffraction on quasi-periodic gratings [23] or the transmission spectra of quasiperiodic photonic crystals [29]. In contrast to the gratings, where there is the spatial modulation, the angular (azimuthal) modulation takes place. Nevertheless, similar to the case of quasi-periodic gratings, a quasiperiod of these modulation superpositions is a reciprocal value of the highest common factor of the modulation frequencies. Here, the role of angular modulation frequencies is played by the OAMs l_1 and l_2. For example, in Figs. 3(a) and 3(c), the highest common factor is 5 and, in both cases, we can see five bright rays diverging from the center that divide the diffraction pattern into identical sectors. Additionally, analysis of calculated phase profiles of these beams reveals the presence of phase singularities as shown in Figs. 4(a) and 4(c) for the binary phase modulation pattern presented in Fig. 2(d). Moreover, intensity distribution in such points tends to zero as shown in Figs. 4(b) and 4(d). These features together indicate the presence of local optical vertices, although their origin is difficult to correspond to the appropriate topological charges in the phase modulation function. The local optical vertices are divided into positive ($l = +1$) and negative ($l = -1$) ones. In particular, it can be seen that the calculated phase distribution has horizontal symmetry, and the phase is twisted around the points on opposite sides from the axis of symmetry. Thus, the vertices from opposite sides have opposite topological charges. It implies that the total OAM is zero, since positive and negative vertices compensate each other.

Each combination of orbital angular momenta (l_n) leads to the formation of a unique diffraction pattern. This approach is not limited to two elements in sum, but can be easily expanded to 3, 4, or any other number of terms, which has been experimentally confirmed. Thus, an almost infinite number of possible combinations with the non-repeating intensity distribution can be obtained.

At $\mathbf{G}_n \neq 0$, a set of different diffraction orders would appear in the pattern. For convenience, we consider the case of three elements in the sum, so that Eq. (2) takes the form

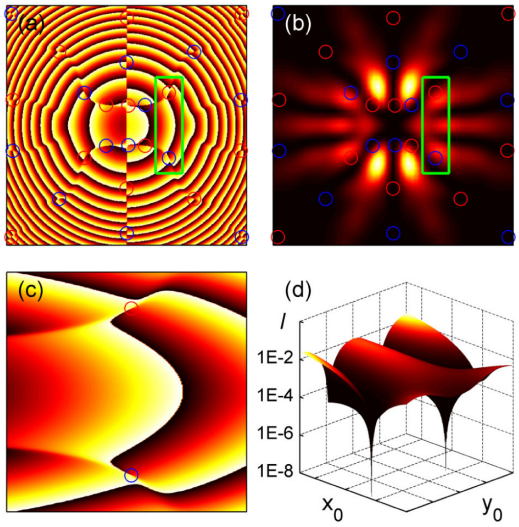

Fig. 4. Calculated phase (a), (c) and intensity (b), (d) distributions for the parameters ($l_1 = 3$, $l_2 = 5$). Red and blue circles represent local optical vertices with positive and negative topological charges, respectively; (c), (d) are regions of interest from plots (a), (b).

$$\Phi(x, \phi) = \Phi_0 + \Delta\Phi \cdot \mathrm{sgn}(a_1 \cos[\mathbf{G}_1 x + l_1\phi] + a_2 \cos[\mathbf{G}_2 x + l_2\phi] + a_3 \cos[\mathbf{G}_3 x + l_3\phi]). \quad \textbf{(3)}$$

In this case, there would be three pronounced maxima corresponding to three $\mathbf{G}_n$ values, and each maximum would have a corresponding OAM equal to l_n (Fig. 5). The extraordinary results were observed at any two RLV equal to each other. It could be expected that, in this case, the maximum at the corresponding spatial frequency obeys the OAM superposition. In fact, these maxima are distorted and, moreover, the remainder maxima with other spatial frequencies are distorted as well. According to the trigonometric formulas, the sum of cosine in Eq. (3) can be represented as the modulation of $\cos[\frac{(\mathbf{G}_1+\mathbf{G}_2)}{2}x + \frac{(l_1+l_2)}{2}\phi]$ by $\cos[(\frac{\mathbf{G}_1-\mathbf{G}_2)}{2}x + \frac{(l_1-l_2)}{2}\phi]$, if $\mathbf{G}_1 = \mathbf{G}_2$; then, the second cosine would be independent of x. Thus, it will produce the azimuthal modulation on the entire BPM pattern.

It is reasonable to form regular and irregular 2D arrays of beams carrying specific OAMs. For this purpose, Eq. (2) can be rewritten in the form

$$\Phi(x, y, \phi) = \Phi_0 + \Delta\Phi \cdot \mathrm{sgn}\left(\sum (a_n \cos[\mathbf{G}_n^x x] + \cos[\mathbf{G}_n^y y + l_n\phi])\right). \quad \textbf{(4)}$$

Thus, the BPM pattern from Eq. (4) will not only multiply the incident beam, but also set specific OAMs for each spatial frequency. In general, the term $l_n\phi$ in Eq. (4) can be added to any cosine (x or y) or both of them simultaneously. Although in the latter case the symmetry axis would not coincide with the x- and y-axis, instead, they would be inclined by an angle corresponding to the ratio between $\mathbf{G}_n^x$ and $\mathbf{G}_n^y$. In addition, in this case, the OAM for each spatial frequency will be a superposition of l_n^x and l_n^y.

The greater the number of maxima in each order, the lower their intensities, while the intensity of the zero non-diffracted order remains unchanged. Therefore, for better observation of the diffraction pattern, the central zero maximum was blocked.

A regular pattern can be obtained if we take $\mathbf{G}_n$ with equal spacings. For example, the regular pattern shown in Fig. 6(a) was obtained at $\mathbf{G}^x = 410; 935; 1460; 1985\ \mathrm{rad}\cdot\mu\mathrm{m}^{-1}$ (spacing is 525) and $\mathbf{G}^y = 415; 840; 1265; 1690; 2115\ \mathrm{rad}\cdot\mu\mathrm{m}^{-1}$ (spacing is 425). If the spacing is equal to $\mathbf{G}_1$, then the first order of the second spatial frequency will intersect with the second order of the first frequency, and the distortion will occur. The intensity distributions for the BPM pattern with random $\mathbf{G}_n^x$ and $\mathbf{G}_n^y$ are shown in Fig. 6(b). Although, one must be careful not to allow different maxima to intersect. Otherwise, these maxima will be strongly distorted, as in the 1D case. In both cases, for the regular and irregular 2D arrays, topological charge l_n was random from 1 to 4. The larger the topological charge, the wider the circle; therefore the intensity will be spread over the larger area, and for better observation, the amplitudes were chosen to be $a_n = 0.25 + l_n/6$.

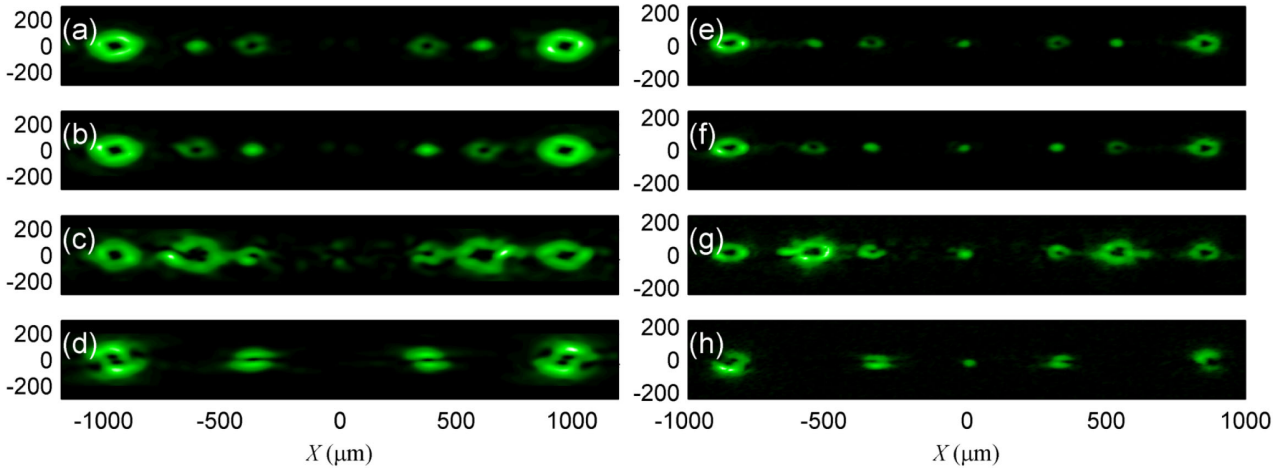

Fig. 5. Calculated (a)–(d) and experimental (e)–(h) diffraction patterns for $G_1 = 0.0436\ \mathrm{rad}\cdot\mu\mathrm{m}^{-1}$, $G_2 = 0.0714\ \mathrm{rad}\cdot\mu\mathrm{m}^{-1}$, and $G_3 = 0.1121\ \mathrm{rad}\cdot\mu\mathrm{m}^{-1}$, and for a set of parameters (a_1, l_1; a_2, l_2; a_3, l_3): (a), (e) (0.5, 1; 0.5, 0; 1, 2); (b), (f) (0.5, 0; 0.5, 1; 1, 2); (c), (g) (0.5, 1; 1.1, 3; 1, 2); and for (d), (h) $G_1 = 0.0436\ \mathrm{rad}\cdot\mu\mathrm{m}^{-1}$, $G_2 = G_3 = 0.1121\ \mathrm{rad}\cdot\mu\mathrm{m}^{-1}$ (0.5, 0; 1, 3; 1, 2).

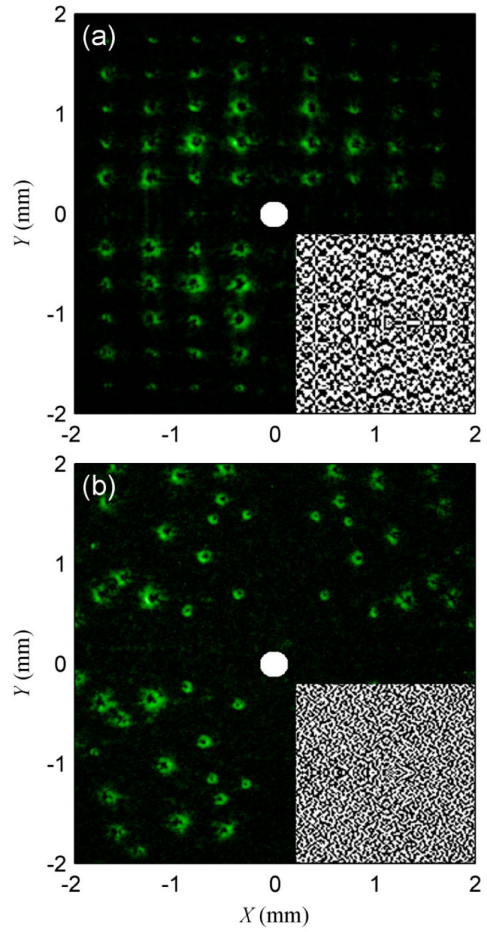

Fig. 6. Experimental diffraction patterns for regular (a) and irregular (b) 2D array of beams. Insets: 2D binary phase masks.

In conclusion, we elaborated and experimentally proved in this Letter a unified approach to controlling the diffraction of beams carrying the orbital angular momentum. Despite some limitations, this analytical approach allows one to control a number of diffraction maxima with the specified orbital angular momenta, intensity distribution between them, and their angular positions by choosing appropriate reciprocal lattice vectors, their amplitudes, and topological charges of a hologram. This analytical method is applicable to creation of 1D and 2D arrays of OAM beams and may provide new opportunities for singular optics.

Funding. Russian Science Foundation (19-12-00203).

Acknowledgment. The authors thank S. A. Myslivets and V. G. Arkhipkin for help with calculations and fruitful discussions.

Disclosures. The authors declare no conflicts of interest.

REFERENCES

1. L. Allen, M. W. Beijersbergen, R. J. C. Spreeuw, and J. P. Woerdman, Phys. Rev. A **45**, 8185 (1992).
2. A. M. Yao and M. J. Padgett, Adv. Opt. Photon. **3**, 161 (2011).
3. Y. Shen, X. Wang, Z. Xie, C. Min, X. Fu, Q. Liu, M. Gong, and X. Yuan, Light Sci. Appl. **8**, 90 (2019).
4. G. Gibson, J. Courtial, and M. J. Padgett, Opt. Express **12**, 5448 (2004).
5. T. Ando, Y. Ohtake, N. Matsumoto, T. Inoue, and N. Fukuchi, Opt. Lett. **34**, 34 (2009).
6. K. Sueda, G. Miyaji, N. Miyanaga, and M. Nakatsuka, Opt. Express **12**, 3548 (2004).
7. L. Marrucci, C. Manzo, and D. Paparo, Phys. Rev. Lett. **96**, 163905 (2006).
8. N. B. Simpson, L. Allen, and M. J. Padgett, J. Mod. Opt. **43**, 2485 (1996).
9. D. G. Grier, Nature **424**, 810 (2003).
10. S. H. Tao, X.-C. Yuan, J. Lin, X. Peng, and H. B. Niu, Opt. Express **13**, 7726 (2005).
11. M. J. Padgett and R. Bowman, Nat. Photonics **5**, 343 (2011).
12. S. Wei, T. Lei, L. Du, C. Zhang, H. Chen, Y. Yang, S. W. Zhu, and X.-C. Yuan, Opt. Express **23**, 30143 (2015).
13. Y. Kozawa, D. Matsunaga, and S. Sato, Optica **5**, 86 (2018).
14. M. Mirhosseini, O. S. Magaña-Loaiza, M. N. O'Sullivan, B. Rodenburg, M. Malik, M. P. J. Lavery, M. J. Padgett, D. J. Gauthier, and R. W. Boyd, New J. Phys. **17**, 033033 (2015).
15. A. Mair, A. Vaziri, G. Weihs, and A. Zeilinger, Nature **412**, 313 (2011).
16. A. C. Dada, J. Leach, G. S. Buller, M. J. Padgett, and E. Andersson, Nat. Phys. **7**, 677 (2011).
17. J. Wang, J.-Y. Yang, I. M. Fazal, N. Ahmed, Y. Yan, H. Huang, Y. Ren, Y. Yue, S. Dolinar, M. Tur, and A. E. Willner, Nat. Photonics **6**, 488 (2012).
18. A. E. Willner, H. Huang, Y. Yan, Y. Ren, N. Ahmed, G. Xie, C. Bao, L. Li, Y. Cao, Z. Zhao, J. Wang, M. P. J. Lavery, M. Tur, S. Ramachandran, A. F. Molisch, N. Ashrafi, and S. Ashrafi, Adv. Opt. Photon. **7**, 66 (2015).
19. T. Lei, M. Zhang, Y. Li, P. Jia, G. N. Liu, X. Xu, Z. Li, C. Min, J. Lin, C. Yu, H. Niu, and X. Yuan, Light Sci. Appl. **4**, e257 (2015).
20. A. Sit, F. Bouchard, R. Fickler, J. Gagnon-Bischoff, H. Larocque, K. Heshami, D. Elser, C. Peuntinger, K. Günthner, B. Heim, C. Marquardt, G. Leuchs, R. W. Boyd, and E. Karimi, Optica **4**, 1006 (2017).
21. S. Fu, Y. Zhai, H. Zhou, J. Zhang, T. Wang, X. Liu, and C. Gao, Opt. Express **27**, 33111 (2019).
22. V. V. Kotlyar, A. A. Kovalev, and A. V. Volyar, Opt. Express **28**, 8266 (2020).
23. D. A. Ikonnikov, V. G. Arkhipkin, and A. M. Vyunishev, Laser Phys. Lett. **16**, 126202 (2019).
24. W. Zhang, J. Tang, P. Chen, G. Cui, Y. Ming, W. Hu, and Y. Lu, Opt. Express **27**, 21667 (2019).
25. S. Fu, Y. Zhai, H. Zhou, J. Zhang, T. Wang, C. Yin, and C. Gao, Opt. Lett. **44**, 4753 (2019).
26. P. Chen, S.-J. Ge, L.-L. Ma, W. Hu, V. G. Chigrinov, and Y.-Q. Lu, Phys. Rev. Appl. **5**, 044009 (2016).
27. D. Marco, M. M. Sánchez-López, A. Cofré, A. Vargas, and I. Moreno, Opt. Express **27**, 14472 (2019).
28. S. Akhmanov and S. Nikitin, *Physical Optics* (Clarendon, 1997).
29. A. M. Vyunishev, P. S. Pankin, S. E. Svyakhovskiy, I. V. Timofeev, and S. Ya. Vetrov, Opt. Lett. **42**, 3602 (2017).